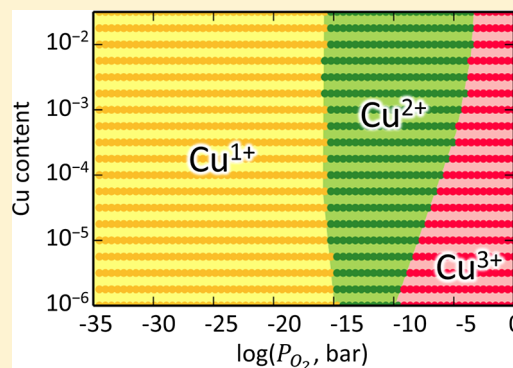


# Solubility Limit of Cu and Factors Governing the Reactivity of Cu–CeO<sub>2</sub> Assessed from First-Principles Defect Chemistry and Thermodynamics

Lixin Sun<sup>†</sup> and Bilge Yildiz<sup>\*,†,‡</sup><sup>†</sup>Laboratory for Electrochemical Interfaces, Department of Nuclear Science and Engineering and <sup>‡</sup>Department of Materials Science and Engineering, Massachusetts Institute of Technology, 77 Massachusetts Avenue, Cambridge 02139, Massachusetts, United States

## Supporting Information

**ABSTRACT:** Cu–CeO<sub>2</sub> is a promising material system for low-temperature water gas shift reactions. The solubility and oxidation state of Cu in Cu–CeO<sub>2</sub> is important for these reactions, but these values have been unclear from the literature to date. We used first-principle calculations and statistical thermodynamics to assess Cu defect configurations and oxidation states in bulk ceria, at both equilibrium and non-equilibrium conditions. Cu solubility was found to be very low, lower than ppm level at equilibrium, indicating that the nanoparticles with high Cu content reported in experimental literature are, in fact, in non-equilibrium states. Thus, these non-equilibrium states were also assessed by fixing the Cu content from 0.001 to 1%. Under oxygen-rich conditions, Cu takes 3+, serving as an acceptor substitutional dopant. Increasing Cu content increases the concentrations of oxygen vacancies and Ce<sup>3+</sup> polarons, which can induce a higher catalytic activity compared to undoped ceria. In addition, with reducing conditions, the oxidation/reduction of the Cu between 1+ and 2+ can also facilitate surface reactions. These findings provide insights into why a higher Cu content can enhance the catalytic activity in Cu–CeO<sub>2</sub>.



## 1. INTRODUCTION

Ceria-based materials, such as Cu–CeO<sub>2</sub>, are promising catalysts for water gas shift (WGS) reaction and preferential oxidation of CO.<sup>1–4</sup> Compared to traditional pyrophoric metal catalysts, ceria-based materials are sulfur tolerant, environmentally friendly, and nonflammable and do not need an activation process.<sup>1</sup> They have the advantage of low cost, high selectivity, and high activity. Although pure ceria alone is a poor catalyst, “doping” ceria with Cu introduces prominent synergic effects on the catalytic activity. Liu and Flytzanistephanopoulos<sup>5</sup> first reported that Cu<sub>0.15</sub>[Ce(La)]<sub>0.85</sub>O<sub>x</sub> nanoparticles synthesized by coprecipitation from aqueous salt solutions can significantly enhance the conversion rate of CO oxidation, compared to pure CeO<sub>2</sub> and pure CuO nanoparticles. The light-off temperature for the CO oxidation reaction is lowered and the CO conversion rate is promoted by an order of magnitude. Cu–CeO<sub>2</sub> catalyst is also found to catalyze low-temperature WGS with higher efficiency.<sup>6</sup>

Cu can appear as a substitution or an interstitial in the ceria lattice and with 1+, 2+, and 3+ oxidation states, but it is unclear which oxidation state of Cu gives rise to the excellent catalytic activity. Here, we review several literatures that report different Cu oxidation states to be the active species, in the order of Cu<sup>1+</sup>, Cu<sup>2+</sup>, and Cu<sup>3+</sup>. Several early works by Flytzani-Stephanopoulos et al.<sup>4,5,7</sup> showed using X-ray photoelectron spectroscopy (XPS) that the dominant active oxidation state of Cu is 1+. Kim et al. also proposed that Cu<sup>1+</sup> substitution is likely the dominant

defect species in Cu–CeO<sub>2</sub> because the ionic radius of Cu<sup>1+</sup> is close to that of Ce<sup>4+</sup>.<sup>8</sup> On the other hand, there are reports suggesting that Cu<sup>2+</sup> may also be the active species. Computational studies by Lu<sup>9</sup> et al. and Kehoe et al.<sup>10</sup> have modeled Cu<sup>2+</sup> substitutional defect in bulk ceria and attributed the high reducibility to the smaller ionic radius of Cu<sup>2+</sup>. They reported that the Cu<sup>2+</sup> substitutional defect can lower the oxygen vacancy formation energy substantially, from 3.28 to 2.39 eV. Therefore, once ceria is doped by Cu, it is more reducible and thus has a better catalytic performance. This result is supported by Bera et al.,<sup>11</sup> who used XPS and electron paramagnetic resonance measurement to find Cu<sup>2+</sup> with octahedral coordination. They also found that the lattice parameter shrinks and attributed this result to the smaller Shannon radii of Cu<sup>2+</sup>. More recently, Wang et al.<sup>12</sup> and Elias et al.<sup>13</sup> reported an even higher oxidation state, Cu<sup>3+</sup>, by X-ray absorption spectroscopy and Raman spectroscopy measurements under oxygen-rich conditions. According to the simulation from Elias et al.<sup>13</sup> Cu<sup>3+</sup> substitutions have a stronger surface segregation tendency and a higher population at the surface and thus should be the origin of the high catalytic activity of Cu–CeO<sub>2</sub>.

All the literature above assumed that Cu acts as a substitutional dopant, which can also increase oxygen vacancy

Received: August 24, 2018

Revised: November 3, 2018

Published: December 5, 2018

concentration and facilitate reactions like water dissociation<sup>14,15</sup> and selective oxidation/reduction. In addition, there are other reports that propose surface oxygen vacancies and “strongly bound Cu–[O<sub>x</sub>]-Ce” complexes to be the active sites for catalytic reactions. Si et al. showed that Cu–[O<sub>x</sub>]-Ce is the active species to catalyze low-temperature WGS.<sup>16</sup> This surface species can form during the WGS reactions by segregating bulk Cu species to the surface.

Moreover, it remains an open question whether the samples used in the experimental studies above were indeed Cu-substituted ceria at equilibrium. In those studies, Cu–CeO<sub>2</sub> samples were synthesized by impregnation,<sup>17</sup> coprecipitation,<sup>18</sup> and combustion techniques,<sup>11,19</sup> involving a relatively low drying temperature ranging from 60 to 400 °C. These temperatures are too low to enable cation diffusion and can kinetically trap the Cu–CeO<sub>2</sub> in a metastable state away from equilibrium. In fact, the Cu–CeO<sub>2</sub> system evolves chemically and topologically at reaction conditions. For example, Knauth et al.<sup>20</sup> performed dilatometry and impedance spectroscopy experiments to find that a Cu<sub>2</sub>O “shell” may form at the surface of the Cu–CeO<sub>2</sub> nanoparticles after annealing at 650 °C. If the sample had been at equilibrium, the solubility of Cu would have increased at higher temperatures and stayed in the CeO<sub>2</sub> lattice, instead of forming a Cu<sub>2</sub>O shell. On the contrary, the previous computational reports reviewed above considered only Cu<sup>2+</sup> substitutional defects, bound with oxygen vacancies, at a fixed (relatively high) concentration and oxidation state of Cu.

The aim of this work is to predict the dominant oxidation state of Cu and its solubility limits in Cu–CeO<sub>2</sub>, as well as implications for catalytic activity at high non-equilibrium concentrations of Cu. As a result, the findings provide insights into consolidating the previous experimental results and computational studies. We use a grand canonical framework<sup>21</sup> to compute the energetics of Cu incorporation into bulk ceria with density functional theory corrected by the Hubbard *U* model (DFT + *U*). The defect formation energies as a function of oxygen chemical potential are then used to calculate the Kröger–Vink diagrams to quantify the concentration of Cu and other defects in ceria. The defect concentrations are computed under equilibrium and non-equilibrium conditions. At equilibrium, the solubility of Cu, estimated by the total concentration of all Cu defects, was found to be much lower than 1 ppm. This low solubility indicates that most Cu–CeO<sub>2</sub> nanoparticles in experiments are, in fact, in non-equilibrium states. For assessing the catalytic implications at high non-equilibrium Cu concentrations, Cu content is fixed at 0.001–1% and the resulting changes in oxidation states and other defect concentrations are assessed. Under oxygen-rich conditions, Cu appears as Cu<sup>3+</sup> substitution. The oxidation state is reduced to 2+ and then 1+ as oxygen partial pressure decreases. In oxidizing environments, Cu<sup>3+</sup> is a substitutional acceptor dopant, which enhances oxygen vacancy concentration. In reducing environments, relevant to the WGS reaction conditions, Cu is an interstitial donor dopant, which enhances Ce<sup>3+</sup> polaron concentration. When the Cu content exceeds 10<sup>−3</sup> and under reducing conditions, 90% of Cu are interstitials with a 1+ oxidation state, whereas 10% of the Cu remain as substitutional defects with a 2+ oxidation state. The substitutional defects are bound with oxygen vacancies. Thus, the oxygen non-stoichiometry can be 10 times higher than in the undoped case even in a reducing environment. Because oxygen vacancies and polarons can promote surface activity of ceria, the Cu doping can enhance the catalytic activity of ceria. In addition,

the oxidation/reduction of the Cu species itself between 1+ and 2+ oxidation states can also facilitate surface reactions.

## 2. METHODS

**2.1. Density Functional Theory Calculations.** The calculations were performed with projector-augmented plane-wave method (PAW) implemented in the Vienna ab initio simulation package (VASP),<sup>22–24</sup> version 5.4.1. We used the generalized gradient approximation (GGA) with the Perdew–Wang 91 (PW91) exchange correlation functional.<sup>25</sup> PW91 was chosen instead of the PBE functional, another more popular GGA exchange correlation functional parameterized by Perdew, Burke, and Ernzerhof,<sup>26</sup> because PW91 offers a more stable and effective convergence of the Ce *f* electrons, as discussed in the later paragraphs. The simulated valence electrons are 5s<sup>2</sup>5p<sup>6</sup>6s<sup>2</sup>5d<sup>1</sup>4f<sup>1</sup> for cerium, 2s<sup>2</sup>2p<sup>6</sup> for oxygen, and 3p<sup>6</sup>3d<sup>10</sup>4p<sup>1</sup> for copper.

In this work, Hubbard *U* correction with Dudarev’s approach<sup>27–29</sup> is applied to Ce *f* and Cu *d* orbitals, with *U*<sub>Ce</sub> = 5 eV and *U*<sub>Cu</sub> = 4 eV. The *U* value for Ce is chosen such that the spin of the *f* orbitals saturates for Ce<sup>3+</sup><sup>30</sup> and the *U* value of Cu is chosen to predict the formation enthalpy of CuO correctly.<sup>31</sup> Applying *U* on oxygen *p* orbitals has also been proposed in the literature to better model hole polarons on oxygen ions.<sup>32</sup> However, because the oxygen hole polaron is not the dominant defect in ceria, oxygen *U* is not used in this work. These *U* values have been successfully used to model the chemical expansion in ceria,<sup>30</sup> surface adsorption properties of reduced ceria,<sup>33</sup> and the band gap and formation enthalpy of CuO and Cu<sub>2</sub>O.<sup>31</sup> In addition, Table S1 in the Supporting Information demonstrates that PW91 performs the same as the PBE functional for the Cu–CeO<sub>2</sub> system, and the oxygen *U* value does not affect the charge localization of Cu defects.

The Hubbard *U* correction also complicates the convergence to the ground state because the penalty function of partial occupation increases the barrier between different meta-stable states, which can trap the system in a local minimum. The DFT algorithm can converge to an arbitrary local minimum that is not energetically favorable.<sup>34</sup> For example, Zacherle et al.<sup>35</sup> reported that the calculation of a neutral oxygen vacancy in ceria with PBE + *U* may converge to a configuration that contains four Ce<sup>3.5+</sup> ions, whereas the lowest energy configuration actually contains two Ce<sup>3+</sup> ions. From the authors’ experience, PW91 performs better than PBE regarding the converge to the Ce<sup>3+</sup> configuration. For all defect calculations, the *U*-ramping technique is also used to guarantee convergence to low-energy configurations.

All defect calculations are performed for a 2 × 2 × 2, 96-atom fluorite structure supercell (Figure S1). A 2 × 2 × 2 Monkhorst–Pack *k*-point mesh with 600 eV energy cutoff and Gaussian smearing with a sigma of 0.05 eV were used. The convergence criterion for ionic relaxation is that the forces on all ions be less than 0.05 eV/Å. The atomic structure is visualized by VESTA<sup>36</sup> and VMD.<sup>37</sup>

**2.2. Defect Formation Energies and Calculation of the Kröger–Vink Diagram.** In this work, the formation of defects as a function of temperature *T* and oxygen partial pressure *P*<sub>O<sub>2</sub></sub> is computed in a grand-canonical framework, which is well summarized in the review by Freysoldt et al.<sup>21</sup> In order to properly account for the defect complex formation, the configurational entropy term is slightly modified compared to the original framework. Details of the derivation can be found in

**Table 1.** Defect Formation Energy (eV) in Bulk CeO<sub>2</sub>, with Cell Pressure  $P = 0^a$ 

defect	site	oxygen rich	oxygen poor	defect	site	oxygen rich	oxygen poor
V <sub>O</sub> <sup>••</sup>		1.32	0.66	(Cu <sub>Ce2</sub> <sup>''</sup> -V <sub>O</sub> <sup>••</sup> ) <sup>x</sup>		2.31	2.95
(V <sub>O</sub> <sup>••</sup> -Ce <sub>Ce</sub> <sup>'</sup> ) <sup>•</sup>		2.04	0.70	(Cu <sub>Ce2</sub> <sup>'''</sup> -V <sub>O</sub> <sup>••</sup> ) <sup>'</sup>		2.98	2.94
(Ce <sub>Ce</sub> <sup>'</sup> -V <sub>O</sub> <sup>••</sup> -Ce <sub>Ce</sub> <sup>'</sup> ) <sup>x</sup>		2.71	0.69	Cu <sub>Ce</sub> <sup>'</sup>	sq	1.73	3.71
Ce <sub>Ce</sub> <sup>'</sup>		1.24	0.55	Cu <sub>Ce</sub> <sup>'</sup>	sub	1.79	3.78
(Cu <sub>i</sub> <sup>•</sup> -Ce <sub>Ce</sub> <sup>'</sup> ) <sup>x</sup>	oct	3.78	2.39	Cu <sub>Ce</sub> <sup>''</sup>	sq	2.00	3.30
Cu <sub>i</sub> <sup>•</sup>	oct	2.83	2.13	Cu <sub>Ce</sub> <sup>''</sup>	sub	2.73	4.03
Cu <sub>i</sub> <sup>••</sup>	oct	3.03	3.01	Cu <sub>Ce</sub> <sup>'''</sup>	sub	3.80	4.41
Cu <sub>i</sub> <sup>••</sup>	sq	3.11	3.09	(Cu <sub>Ce</sub> <sup>''</sup> -Ce <sub>Ce</sub> <sup>'</sup> ) <sup>'''</sup>	sq	2.82	3.44
Cu <sub>i</sub> <sup>•••</sup>	oct	3.84	4.50	Cu <sub>O</sub> <sup>••</sup>		6.83	4.78
Cu <sub>i</sub> <sup>•••</sup>	sq	3.83	4.49	Cu <sub>O</sub> <sup>•••</sup>		6.36	5.00
O <sub>i</sub> <sup>''</sup>		3.09	3.75	Cu <sub>O</sub> <sup>••••</sup>		7.93	7.25
				Cu <sub>O</sub> <sup>•••••</sup>		7.40	7.40

<sup>a</sup>The formation energy is computed under both oxygen-rich conditions,  $\Delta\mu_{\text{O}} = 0$  eV,  $\Delta\mu_{\text{Cu}} = -1.4$  eV,  $\mu_{\text{e}} = 0.7$  eV, and oxygen-poor conditions,  $\Delta\mu_{\text{O}} = -2.0$  eV,  $\Delta\mu_{\text{Cu}} = 0$  eV,  $\mu_{\text{e}} = 1.4$  eV at 400 °C. “sq” stands for square planar site in the center of a four-oxygen plane; “sub” stands for Ce site; “oct” stands for octahedral site in the Ce fcc lattice. Energy unit: eV.

the [Supporting Information](#). The free-energy per unit formula for CeO<sub>2</sub> can be written as

$$\begin{aligned}
 g &= \frac{G}{N_{\text{S}}} \\
 &= \sum_{i=1}^{n_{\text{X}}} c_{\text{X}_i} E_{\text{X}_i}^{\text{f}} + \sum_L \sum_{i=1}^{n_L} c_{L_i} E_{L_i}^{\text{f}} \\
 &\quad + k_{\text{B}} T \left\{ \sum_{i=1}^{n_{\text{X}}} (c_{\text{X}_i} \ln c_{\text{X}_i} - c_{\text{X}_i} \ln f_{\text{X}_i}) + \left( 1 - \sum_{i=1}^{n_{\text{X}}} c_{\text{X}_i} \right) \right. \\
 &\quad \ln \left( 1 - \sum_{i=1}^{n_{\text{X}}} c_{\text{X}_i} \right) + \sum_L \left[ \sum_{i=1}^{n_L} c_{L_i} \ln \frac{c_{L_i}}{z_L - \sum_{i=1}^{n_{\text{X}}} z_L^{\text{X}_i} c_{\text{X}_i}} \right. \\
 &\quad \left. \left. + \left( z_L - \sum_{i=1}^{n_{\text{X}}} z_L^{\text{X}_i} c_{\text{X}_i} - \sum_{i=1}^{n_L} c_{L_i} \right) \ln \left( 1 - \frac{\sum_{i=1}^{n_L} c_{L_i}}{z_L - \sum_{i=1}^{n_{\text{X}}} z_L^{\text{X}_i} c_{\text{X}_i}} \right) \right] \right\} \quad (1)
 \end{aligned}$$

Here, we use the following notation:  $E_{L_i}^{\text{f}}$  and  $c_{L_i}$  denote the formation energy and the defect concentration of point defect  $L_i$  at sublattice  $L$  ( $L$  = cation, anion, square planar interstitial and octahedral interstitial lattice), respectively.  $E_{\text{X}_i}^{\text{f}}$  and  $c_{\text{X}_i}$  are the formation energy and the concentration of defect complex  $\text{X}_i$ , respectively.  $z_L$  is the number of available sites per CeO<sub>2</sub> formula for sublattice  $L$ , and  $z_L^{\text{X}_i}$  is the number of  $L$  lattice sites occupied by one  $\text{X}_i$ .

The equilibrium defect concentrations can be solved from  $\frac{\partial g}{\partial c_{\text{d}}} = 0$

$$c_{L_i} = \left( z_L - \sum_{i=1}^{n_{\text{X}}} z_L^{\text{X}_i} c_{\text{X}_i} \right) \frac{e^{-E_{L_i}/k_{\text{B}}T}}{1 + W_L} \quad (2)$$

$$c_{\text{X}_i} = \frac{f_{\text{X}_i} e^{-E_{\text{X}_i}/k_{\text{B}}T} \prod_L (1 + W_L)^{-z_L^{\text{X}_i}}}{1 + W_{\text{X}}} \quad (3)$$

$$W_{\text{X}} = \sum_{i=1}^{n_{\text{X}}} \left( f_{\text{X}_i} e^{-E_{\text{X}_i}/k_{\text{B}}T} \prod_L \left( 1 + \sum_{i=1}^{n_L} e^{-E_{L_i}/k_{\text{B}}T} \right)^{-z_L^{\text{X}_i}} \right) \quad (4)$$

$$W_L = \sum_{i=1}^{n_L} e^{-E_{L_i}/k_{\text{B}}T} \quad (5)$$

The details of the derivation and reference chemical potentials for oxygen and Cu are listed in the [Supporting Information](#).

In this formulation, the defect–defect interaction is handled in two parts. The defect–defect attraction is explicitly computed by the energy term  $\sum_{i=1}^{n_{\text{X}}} c_{\text{X}_i} E_{\text{X}_i}^{\text{f}}$ , and the repulsion is implicitly modeled by counting the site competition in the configurational entropy. If a defect complex has a positive binding energy, the  $c_{\text{X}_i} E_{\text{X}_i}^{\text{f}}$  term competes with the point defects that make up this complex. The complex concentration can be higher than that of the point defects when they have a positive binding energy and the isolated species concentrations are high enough. If there are several species that occupy the sites in the same lattice, the configurational entropy term will prevent double occupation in the same site. If there are no defect–defect interactions and the defect concentrations are within the dilute limit, [eqs 2 and 3](#) will not contain any  $c_{\text{X}_i}$  terms and the dilute solution is recovered.

We note that this formulation is essentially similar to a simplified cluster expansion with only nearest neighbor pairwise and three-body interactions. The fact that long-range interaction is missing in the Gibbs free energy limits the prediction accuracy at high defect concentrations (>1%). Yet, the benchmark shown in the [Supporting Information](#) demonstrates that the prediction of this framework is comparable to experimental measurement in undoped ceria.

### 3. RESULTS AND DISCUSSION

**3.1. Formation Energies and Configurations of Cu Defects.** Copper atoms can be incorporated into the ceria lattice as point defects. We investigate the energetics of Cu atoms in ceria as interstitials, substitutional defects at a cerium site or an oxygen site, and as part of a defect complex. For each type of defect, several possible structures and oxidation states are examined to determine the lowest energy structure. All defect formation energies under oxygen-poor and oxygen-rich conditions are listed in [Table 1](#).

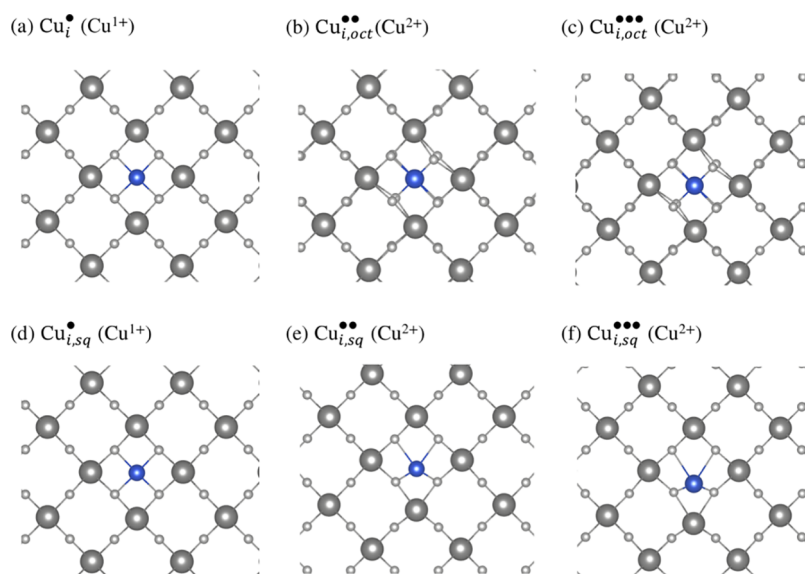


**Figure 1.** Relaxed configurations of Cu interstitials in bulk CeO<sub>2</sub>. The large gray, small gray, and blue spheres represent Ce, O, and Cu atoms, respectively. For clarity, only one (001) plane of Ce and two (001) planes of oxygen are shown. The viewing direction is  $\langle 100 \rangle$ .

**Table 2.** Bader Charge and Bader Spin of Cu Atoms in Different Defect Configurations in Bulk Ceria<sup>a</sup>

defect	oxidation state	Bader charge ( $e$ )	Bader spin ( $\mu_B$ )	defect	oxidation state	Bader charge ( $e$ )	Bader spin ( $\mu_B$ )
*Cu <sub>i,oct</sub> <sup>•</sup>	1+	0.59	0	Cu <sub>Ce,sub</sub> <sup>'''</sup>	1+	0.90	0
*Cu <sub>i,oct</sub> <sup>••</sup>	2+	0.73	0.50	*(Cu <sub>Ce,sq</sub> <sup>''</sup> —Ce <sub>Ce</sub> <sup>'''</sup> )	2+	1.05	0.61
Cu <sub>i,sq</sub> <sup>••</sup>	2+	0.77	0.47	Cu <sub>Ce,sub</sub> <sup>''</sup>	2+	1.10	0.48
*Cu <sub>i,oct</sub> <sup>•••</sup>	2+	0.74	0.50	*Cu <sub>Ce,sq</sub> <sup>''</sup>	2+	1.22	0.62
Cu <sub>i,sq</sub> <sup>•••</sup>	3+	0.97	0	Cu <sub>Ce,sub</sub> <sup>'</sup>	2+	1.30	0.76
				*Cu <sub>Ce,sq</sub> <sup>'</sup>	3+	1.20	0

<sup>a</sup>“\*” indicates a lower formation energy.

**3.1.1. Cu Interstitials.** We investigate three charge states and two interstitial sites, Cu<sub>i,s</sub><sup>•</sup>, Cu<sub>i,s</sub><sup>••</sup>, and Cu<sub>i,s</sub><sup>•••</sup>, where  $s = \text{oct}$  or  $\text{sq}$ . A site-oct interstitial occurs at the octahedral interstitial site of the Ce fcc sublattice; this interstitial is coordinated to eight oxygen ions in the first neighbor shell and six Ce atoms in the second neighbor shell. A site-sq interstitial occurs at a square-planar site; it is coordinated to four oxygen ions at a plane, which is close to the coordination environment for Cu in LaCuO<sub>2</sub>.

The relaxed atomic configurations of all six structures are plotted in Figure 1. When the interstitial is singly charged, the Cu<sub>i</sub><sup>•</sup> always relaxes to an eightfold coordinated site regardless of its initial position (Figure 1a,d). The surrounding atoms barely move compared to the undoped ceria without any Cu<sub>i</sub><sup>•</sup>. When the interstitial is doubly charged, the formation energy of Cu<sub>i,oct</sub><sup>••</sup> is 0.13 eV lower than that of Cu<sub>i,sq</sub><sup>••</sup>. For the eightfold coordinated Cu<sub>i,oct</sub><sup>••</sup> as shown in Figure 1b, two Cu—O bonds are shorter ( $d_{\text{Cu—O}} = 1.99 \text{ \AA}$ ) than the remaining six Cu—O bonds ( $d_{\text{Cu—O}} = 2.4 \text{ \AA}$ ). For the fourfold coordinated Cu<sub>i,sq</sub><sup>••</sup> as shown in Figure 1e, the interstitial repels its nearest Ce<sup>4+</sup> ion, moving away from the CuO<sub>4</sub> plane and displacing its nearest Ce<sup>4+</sup> atom as well. When the interstitial is triply charged, the formation energy of Cu<sub>i,oct</sub><sup>•••</sup> and Cu<sub>i,sq</sub><sup>•••</sup> is different only by 0.01 eV. The relaxation structures of Cu<sub>i,1</sub><sup>•••</sup> and Cu<sub>i,2</sub><sup>•••</sup> are similar to the ones of Cu<sub>i,oct</sub><sup>••</sup> and Cu<sub>i,sq</sub><sup>••</sup> except that the Ce—Cu distance in Cu<sub>i,oct</sub><sup>•••</sup> is slightly larger than that in Cu<sub>i,sq</sub><sup>•••</sup>. These two configurations are depicted in Figure 1d,f.

The oxidation state of the Cu atom in these interstitial configurations can be derived by comparing their partial charges and spins from Bader charge analysis (Table 2) and the spin

density contour plotted in Figure 2. As evident from Table 2, the Bader charge increases as the charge state of the interstitial increases. This trend suggests that the oxidation state of Cu is 1+ for Cu<sub>i,oct</sub><sup>•</sup>, 2+ for Cu<sub>i,oct</sub><sup>••</sup> or  $\text{sq}$ , and 3+ for Cu<sub>i,sq</sub><sup>•••</sup>. For Cu<sub>i,oct</sub><sup>•</sup> the Cu atom does not have spin, which is consistent with its electronic

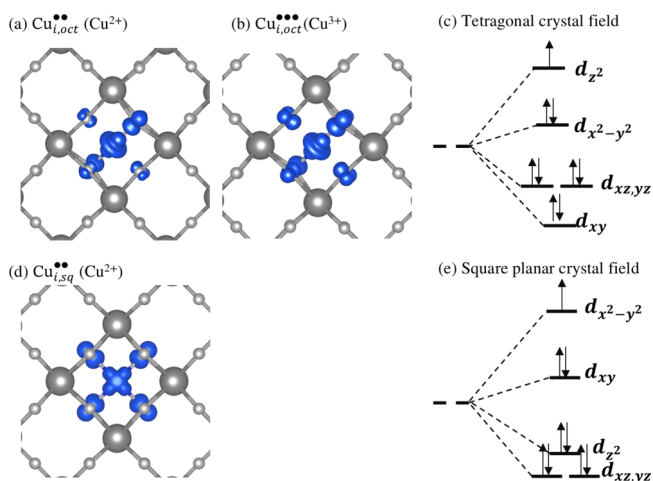


**Figure 2.** (a,b) (d) Spin density contour of Cu interstitials in CeO<sub>2</sub>. The blue surface is an isosurface of  $0.05 \text{ e/\AA}^3$ . The large gray, small gray, and blue spheres represent Ce, O, and Cu atoms, respectively. (c,e) Schematic of d orbital splitting, (c) under a tetragonal and (e) under a square planar crystal field. For clarity, only one (001) plane of Ce and two (001) planes of oxygen are shown. The viewing direction is  $\langle 100 \rangle$ .

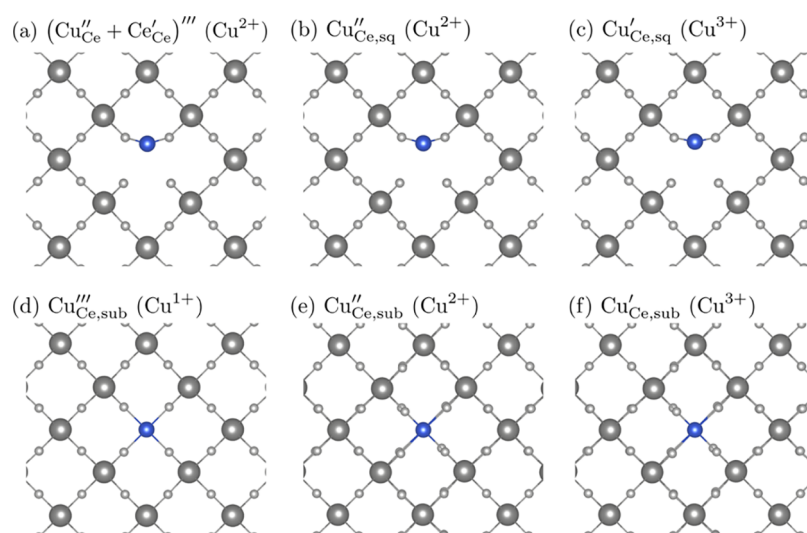


**Figure 3.** Relaxed configurations of  $\text{Cu}_{\text{Ce}}$  substitutional defects in bulk  $\text{CeO}_2$ . The large gray, small gray, and blue spheres represent Ce, O, and Cu atoms, respectively. For clarity, only one (001) plane of Ce and two (001) planes of oxygen are shown. The viewing direction is  $\langle 100 \rangle$ .

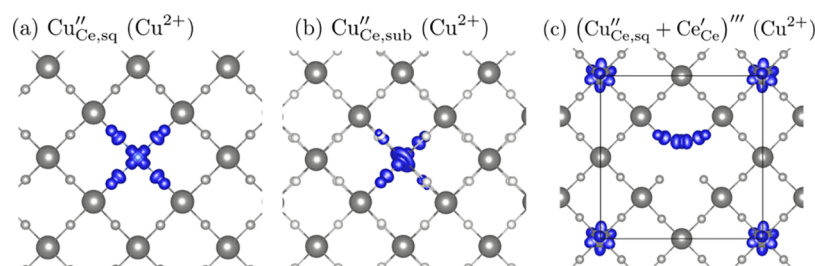


**Figure 4.** Spin density contour of Cu substitutional in  $\text{CeO}_2$ . The blue surface is the isosurface of  $0.05 \text{ e}/\text{\AA}^3$ . The large gray, small gray, and blue spheres represent Ce, O, and Cu atoms, respectively. For clarity, only one {001} plane of Ce and two {001} planes of oxygen are shown. The viewing direction is  $[100]$ .

configuration,  $[\text{Ar}]3\text{d}^{10}$ . For  $\text{Cu}_{i,\text{oct}}^{\bullet\bullet}$ , the Bader spin and its spin density contour (Figure 2a) is consistent with an  $[\text{Ar}]3\text{d}^9$  ion under Jahn–Teller distortion. It can be seen in Figure 2b that two oxygen ions are closer to Cu than the six remaining oxygen ions, leading to a tetragonal crystal field around the Cu (Figure 2c). This symmetry shifts  $d_z^2$  to the highest energy among all 3d orbitals. The spin density around  $\text{Cu}_{i,\text{oct}}^{\bullet\bullet}$  has the shape of the  $d_z^2$  orbital, displayed in Figure 2a. Similarly,  $\text{Cu}_{i,\text{sq}}^{\bullet\bullet}$  has a square-planar crystal field (Figure 2e). The spin contour of this interstitial (Figure 2d) is the same as the highest energy d orbital  $d_{x^2-y^2}$ . Therefore, one can unambiguously confirm that  $\text{Cu}_{i,\text{oct}}^{\bullet\bullet}$  and  $\text{Cu}_{i,\text{sq}}^{\bullet\bullet}$  are both  $\text{Cu}^{2+}$  ions. For  $\text{Cu}_{i,\text{sq}}^{\bullet\bullet\bullet}$ , there is no spin density on Cu, which is consistent with  $[\text{Ar}]3\text{d}^8$ .

However,  $\text{Cu}_{i,\text{oct}}^{\bullet\bullet\bullet}$  is an exception to the trend of increasing Bader charge for a higher oxidation state. The Bader spin and Bader charge of Cu are the same as that of the Cu in  $\text{Cu}_{i,\text{oct}}^{\bullet\bullet}$ . The only difference is that the oxygen neighbor has a stronger spin component, which means that  $\text{Cu}_{i,\text{oct}}^{\bullet\bullet\bullet}$  is actually  $\text{Cu}^{2+}$  with ligand holes on oxygen.

**3.1.2. Cu Substitutional Defects.** Similar to interstitial defects, we model Cu substitutional defect, including  $\text{Cu}_{\text{Ce}}$  and  $\text{Cu}_{\text{O}}$ .  $\text{Cu}_{\text{O}}$  is a Cu atom replacing a host O atom. It is very unlikely to form because of its high charge state, so we list only the energetics of  $\text{Cu}_{\text{O}}$  in Table 1.  $\text{Cu}_{\text{Ce}}$  is a Cu atom replacing a host Ce atom. The site of this Cu atom can be at the original site of Ce, labeled as site sub, or the square planar site labeled as site sq, the same as the site sq discussed in the previous section.

For all three charge states, the substitutional defect prefers the fourfold coordinated site sq to the eightfold coordinated site sub. The formation energies of site sq are 0.06, 0.74 and 0.98 eV lower than those of the site sub, for singly charged  $\text{Cu}_{\text{Ce}}'$ , doubly charged  $\text{Cu}_{\text{Ce}}''$ , and triply charged  $\text{Cu}_{\text{Ce}}'''$ , respectively. The relaxed configurations are plotted in Figure 3. In the site sq configurations (Figure 3a–c), the Cu atom slightly deviates from the  $\text{CuO}_4$  plane, but not as much as seen in the interstitial defect  $\text{Cu}_{i,\text{sq}}$ . In the site sub configurations (Figure 3d–f), the Jahn–Teller distortion was observed for  $\text{Cu}_{\text{Ce},\text{sub}}''$  and  $\text{Cu}_{\text{Ce},\text{sub}}'$ . More interestingly, during the structural optimization of  $\text{Cu}_{\text{Ce},\text{sq}}'$ , an f electron localizes at a Ce atom, forming a defect complex  $(\text{Cu}_{\text{Ce}}' - \text{Ce}_{\text{Ce}}''')'''$  in the end. The formation energy of this defect complex is still lower than the site sub defect  $\text{Cu}_{\text{Ce},\text{sub}}'''$ .

From the Bader spin in Table 2 and spin contour in Figure 4, the oxidation state of Cu substitutional in these configurations can be determined as 1+ for  $\text{Cu}_{\text{Ce},1}'''$ ; 2+ for  $\text{Cu}_{\text{Ce},3}''$ ,  $\text{Cu}_{\text{Ce},2}''$ , and  $\text{Cu}_{\text{Ce},3}'$ ; and 3+ for  $\text{Cu}_{\text{Ce},2}'$ .  $\text{Cu}_{\text{Ce}}$  generally has a larger Bader charge than  $\text{Cu}_i$  because there is more open space around  $\text{Cu}_{\text{Ce}}$  in these configurations. The Bader charge and spin of  $\text{Cu}_{\text{Ce}}$  are also more sensitive to the coordination environment than those of interstitial defects. For example,  $(\text{Cu}_{\text{Ce}}' - \text{Ce}_{\text{Ce}}''')'''$ ,  $\text{Cu}_{\text{Ce},\text{sub}}''$ ,  $\text{Cu}_{\text{Ce},\text{sq}}''$ , and  $\text{Cu}_{\text{Ce},\text{sub}}'$  all contain  $\text{Cu}^{2+}$ , but their Bader charge ranges from 1.05 to 1.30 and their Bader spin ranges from 0.48 to 0.76. Their oxidation states are determined to be 2+ because only one or no  $\text{Ce}^{3+}$  is found in these configurations.

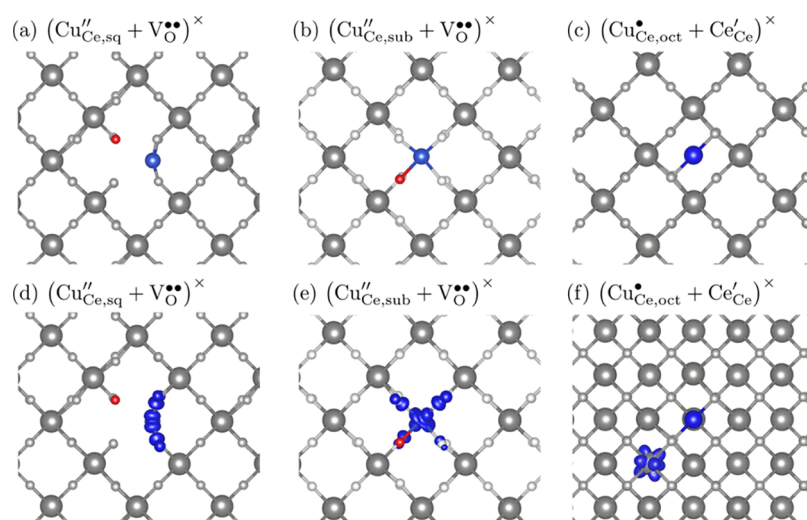


**Figure 5.** (a–c) Relaxed configurations and (d–f) spin density of defect complexes. The large gray, small gray, red, and blue spheres represent Ce, O,  $V_O$ , and Cu atoms, respectively. For clarity, only one (001) plane of Ce and two (001) planes of oxygen are shown in (a–e); three (001) planes of O and two (001) planes of Ce are shown in (f). The viewing direction is  $\langle 100 \rangle$ .

**3.1.3. Cu Defect Complex.** Two defect complexes were investigated,  $Cu_i - Ce'_{Ce}$  and  $Cu_{Ce} - V_O^{••}$ . The relaxation and spin density are all similar to the interstitial, shown in Figure 5.

For the  $Cu_{Ce} - V_O^{••}$  complex, only  $Cu^{2+}$  and  $Cu^{3+}$  can be stabilized, which are labeled as  $(Cu_{Ce}'' - V_O^{••})^x$  and  $(Cu_{Ce}' - V_O^{••})^{\bullet}$ , respectively. In the  $(Cu_{Ce}'' - V_O^{••})^x$  configuration, one electron of the  $Cu^{1+}$  substitution will transfer to a Ce, which is actually  $(Cu_{Ce}'' - Ce'_{Ce} - V_O^{••})^x$ . For the  $(Cu_{Ce}' - V_O^{••})^{\bullet}$  case, two substitutional sites, sq and sub, are investigated. The square-planar site has a 0.74 eV lower formation energy than the substitutional site. For  $Cu_i - Ce'_{Ce}$  complex, only  $Cu^{1+}$  at an octahedral site can be stabilized, which is labeled as  $(Cu_{i,oct}^* - Ce'_{Ce})^x$ .

The binding energy of all defect complexes are positive, as listed in Table 3. The vacancy–substitution complex,  $Cu_{Ce} -$

$V_O^{••}$ , has a high energy  $>1$  eV. However, the binding energy itself is not enough to predict whether a defect complex will dominate. It is only a measure of how likely it is that the point defects are bound together. Section 3.1.1 will show that these defect complexes emerge only when their point defect components are concentrated enough.

**3.1.4. Thermodynamic Transition Levels.** The defect formation energy as a function of electron chemical potential at  $P_{O_2} = 1$  atm and 800 °C is plotted in Figure 6.

The oxidation state of the Cu interstitial is  $2+$  ( $Cu_i^{2+}$ ) at low  $\mu_F$  and  $1+$  ( $Cu_i^+$ ) when  $\mu_F > 0.43$  eV. The oxidation state of the Cu substitutional is  $3+$  ( $Cu_{Ce}^{3+}$ ) at low  $\mu_F$  and  $2+$  ( $Cu_{Ce}^{2+}$ ) when  $\mu_F > 1.01$  eV. When the substitutional defect binds with an oxygen vacancy ( $Cu_{Ce} - V_O^{••}$ ), the Cu oxidation state is  $2+$ .

Interestingly, when the electron chemical potential is close to the  $Ce^{3+}$  in-gap state position ( $\mu_e = 1.6$  eV), every defect loses at least one electron to its nearest Ce cation, forming  $Ce^{3+}$ . For example,  $Cu^0$  interstitial does not exist. Instead, it rather forms a defect complex of  $(Cu_{i,oct}^* - Ce'_{Ce})^x$ , which consists of one  $Cu^{1+}$  and one  $Ce^{3+}$ .

**3.2. Defect Concentrations in Cu-Doped  $CeO_2$  at Equilibrium and Nonequilibrium Conditions.** The defect

**Table 3.** Binding Energy of Charged Defects in Bulk Ceria

defect	binding energy (eV)	defect	binding energy (eV)
$(Ce_{Ce}' - V_O^{••} - Ce_{Ce}')^x$	1.07	$(Cu_{Ce}'' - Ce_{Ce}')^x$	0.26
$(V_O^{••} - Ce_{Ce}')^{\bullet}$	0.50	$(Cu_{Ce,sq}'' - V_O^{••})^x$	1.00
$(Cu_{i,oct}^* - Ce_{Ce}')^x$	0.29	$(Cu_{Ce,2}' - V_O^{••})^{\bullet}$	1.69

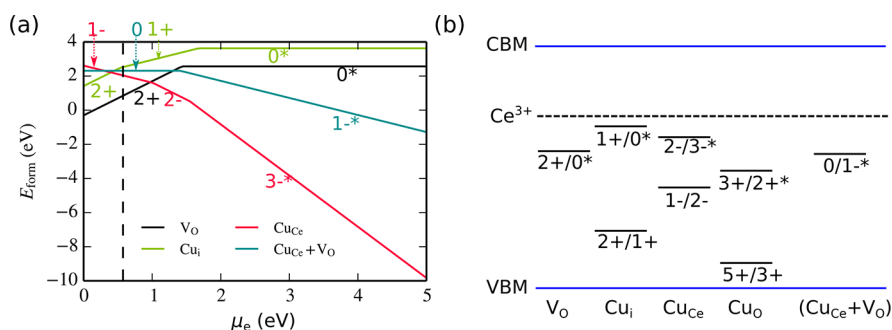


**Figure 6.** (a) Defect formation energies as a function of the electron chemical potential  $\mu_e$  at 400 °C and  $P_{O_2} = 1$  bar. (b) Thermodynamic transition levels for intrinsic and Cu defects. The initial and final states of the transition are marked as the first and second number under each line, respectively. The black dashed line marks the level of the polaron state for  $Ce^{3+}$ , whereas the blue lines represent the DFT +  $U$  computed conduction band minimum and valence band maximum. The (\*) sign means the defect is bound with polarons. For example, a  $0^*$  charge state for  $V_O$  consists of a  $V_O^{••}$  and two  $Ce'_{Ce}$ .

concentration as a function of oxygen partial pressure (Kröger–Vink diagram) is computed for both equilibrium and non-equilibrium states, for  $\text{Cu}_x\text{Ce}_{1-x}\text{O}_{2-\delta}$  at 400 °C. This temperature is a typical calcination temperature for coprecipitation and catalyst regeneration.<sup>16</sup> The Cu solubility can be solved from the total concentration of all Cu defects in equilibrium state. However, as stated in the Introduction, the experimental samples may not reach true equilibrium because of the slow kinetics at low temperatures used in experimental studies. Therefore, the non-equilibrium state with a rather high Cu concentration is also computed.

**3.2.1. Equilibrium State.** In equilibrium state, the Cu chemical potential is computed by subtracting the oxygen chemical potential from the formation energy of CuO,  $\text{Cu}_2\text{O}$ , and Cu metal,

$$\mu_{\text{Cu}} = \min_{(x,y)=(2,1), (1,1) \text{ and } (1,0)} \left\{ \frac{1}{x} \left( E_{\text{Cu}_x\text{O}_y}^{\text{DFT}+U} - \frac{y}{2} \mu_{\text{O}_2} \right) \right\}.$$

This represents the true equilibrium between ceria and Cu/ $\text{Cu}_2\text{O}$ /CuO. The dominant Cu defects, whose concentration is larger than  $10^{-20}$  per unit formula, are plotted in Figure 7. Cu appears as a substitutional defect under oxygen-rich conditions and an interstitial defect under oxygen-poor conditions.

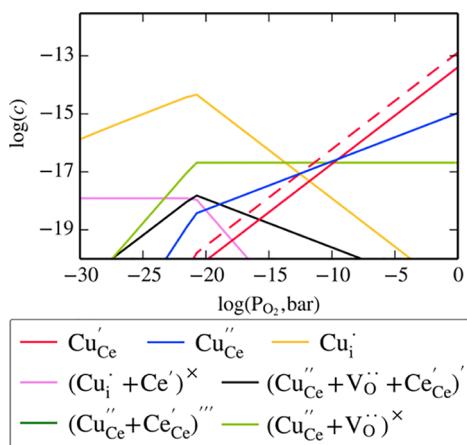


**Figure 7.** Defect concentrations,  $c$ , per unit formula, as a function of  $P_{\text{O}_2}$  in  $\text{Cu}-\text{CeO}_2$  at 400 °C. Only the dominant Cu defect species whose concentration is larger than  $10^{-20}$  per unit formula are shown. Dashed lines represent the square-planar Cu configurations; solid lines represent octahedral interstitials or direct substitutional defects.

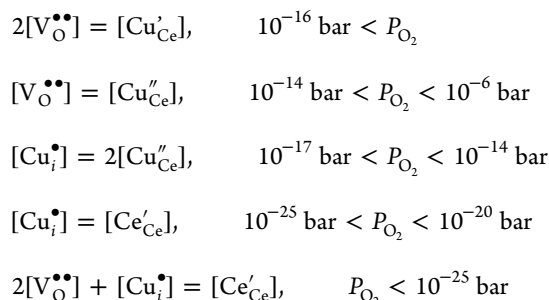
None of the copper defect concentrations exceed 1 ppm, indicating a very low Cu solubility ( $x < 10^{-11}$  in  $\text{Cu}_x\text{Ce}_{1-x}\text{O}_{2-\delta}$ ). The Cu concentration is negligible when compared to the intrinsic defect concentration in the undoped ceria, around 1 ppm under oxygen-rich conditions ( $P_{\text{O}_2} = 1$  bar) and 1% under oxygen-poor conditions. This low Cu solubility is consistent with a previous computational study by Vanpoucke et al., which shows Cu-doped ceria phase can be unstable.<sup>38</sup> Because of such a low Cu solubility, the intrinsic defects remain unchanged. This result is contrary to all those of previous experimental studies, which defined Cu– $\text{CeO}_2$  as Cu-doped ceria, with a Cu concentration as high as 10%.<sup>4,7,11,13,16</sup> However, as pointed out in the Introduction, most of the samples were synthesized at relatively low drying temperatures, which did not allow the sample to fully equilibrate. Moreover, the samples were also nanoparticles with a high surface area, instead of bulk ceria. As a result, these experimental samples and data do not necessarily

reflect the thermodynamic equilibrium of the bulk Cu– $\text{CeO}_2$  system.

**3.2.2. Nonequilibrium State.** Although the Cu content is negligible in  $\text{CeO}_2$  at equilibrium, it can be forced into ceria beyond the solubility limits, trapped at non-equilibrium states. The Cu concentration in these nanoparticles is maintained at the level of 1–10%, which we believe to be far from equilibrium based on results above predicting equilibrium Cu concentrations in  $\text{CeO}_2$  to be below ppm level. The highly concentrated Cu can then impact the concentration of other defects, such as oxygen vacancies, and ultimately impact the catalytic performance of Cu– $\text{CeO}_2$ . In order to analyze the impact of Cu in  $\text{Cu}_x\text{Ce}_{1-x}\text{O}_2$  under these conditions, the Kröger–Vink diagram is also computed for a fixed total Cu concentration up to 1% ( $x = 10^{-2}$ ) as a function of  $P_{\text{O}_2}$  at a typical calcination temperature, 400 °C.

Figure 8a shows the major Cu defects whose concentrations exceed  $10^{-8}$  per unit formula for  $\text{Cu}_x\text{Ce}_{1-x}\text{O}_{2-\delta}$ ,  $x = 10^{-5}$ . From high  $P_{\text{O}_2}$  to low  $P_{\text{O}_2}$ , the dominant Cu defects are first  $\text{Cu}'_{\text{Ce}}$ , then  $(\text{Cu}''_{\text{Ce}} - \text{V}_\text{O}^{\bullet\bullet})^x$ , and finally  $\text{Cu}_i^{\bullet}$ . The oxidation states for these three defects are 3+, 2+, and 1+, respectively.

The charge compensation mechanisms can be described by the following equations.



Therefore, the concentration of doubly charged oxygen vacancies  $\text{V}_\text{O}^{\bullet\bullet}$  is raised by  $\text{Cu}'_{\text{Ce}}$  at high  $P_{\text{O}_2}$  and decreased by  $\text{Cu}_i^{\bullet}$  at low  $P_{\text{O}_2}$ . The vacancy concentration for  $x = 10^{-5}$  is compared with undoped ceria ( $x = 0$ ) in Figure 8c. In undoped ceria, the concentration of the oxygen vacancy monotonically increases as  $P_{\text{O}_2}$  decreases. In Cu-doped ceria, the vacancy has a V-shaped dependence. At high  $P_{\text{O}_2}$ ,  $\text{Cu}'_{\text{Ce}}$  and  $\text{Cu}''_{\text{Ce}}$  introduce extrinsic vacancies for charge compensation. At decreased  $P_{\text{O}_2}$ ,  $\text{V}_\text{O}^{\bullet\bullet}$  concentration drops because most of them were bound with  $\text{Cu}''_{\text{Ce}}$  to form the defect complex  $(\text{Cu}''_{\text{Ce}} - \text{V}_\text{O}^{\bullet\bullet})^x$ . The vacancy concentration continues to decrease until the intrinsic vacancy concentration is high enough to dominate. Polarons are negative defects. Thus, they have a lower concentration than undoped ceria under oxygen-rich conditions and a higher concentration than undoped ceria under oxygen-poor conditions, as shown in Figure 8d.

As a result, the overall non-stoichiometry  $\delta$  in doped ceria deviates from the  $\delta$  of undoped ceria ( $x = 0$ ). As shown in Figure 8e, for  $10^{-8} < x < 10^{-4}$ ,  $\delta$  is higher than in undoped ceria at  $P_{\text{O}_2} > 10^{-17}$  bar. The high  $\delta$  is caused by  $\text{Cu}'_{\text{Ce}}$  and  $(\text{Cu}''_{\text{Ce}} - \text{V}_\text{O}^{\bullet\bullet})^x$  introducing extrinsic vacancies. The overall polaron concentration has the opposite trend: it is lower than in the undoped case at  $P_{\text{O}_2} > 10^{-13}$  and higher than in the undoped case at  $P_{\text{O}_2} < 10^{-13}$ .

For  $x = 10^{-2}$ , Figure 8b shows that the dominant Cu defects at different  $P_{\text{O}_2}$  is similar to  $x = 10^{-5}$ . Because the overall defect concentration is much higher in this case, even the non-

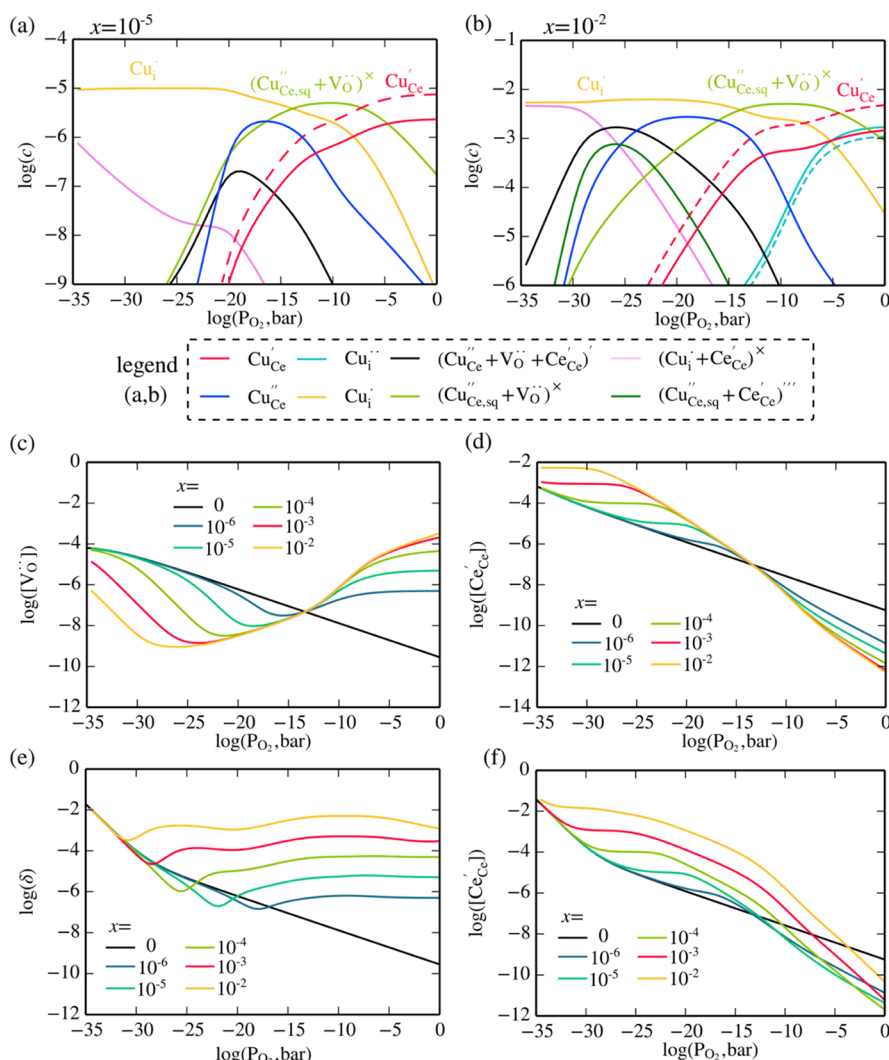
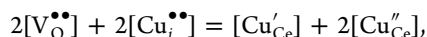
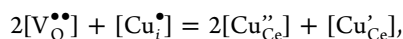


**Figure 8.** Major Cu defect species as a function of  $P_{O_2}$  in  $Cu_xCe_{1-x}O_{2-\delta}$  for (a)  $x = 10^{-5}$  and (b)  $x = 10^{-2}$ . Dashed lines represent the square-planar Cu configurations; solid lines represent octahedral interstitials or direct substitutional defects. (c) Isolated doubly charged oxygen vacancy concentration as a function of  $x$ . (d) Isolated polaron concentration as a function of  $x$ . (e) Overall oxygen non-stoichiometry,  $\delta$ . (f) Overall polaron concentration, including the ones bound with other point defects. All data were computed at 400 °C. Defect concentration unit is per formula.

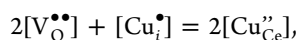
dominant species have substantial concentrations. Thus, the charge compensation mechanisms are more complicated.



$$10^{-5} \text{ bar} < P_{O_2}$$



$$10^{-15} \text{ bar} < P_{O_2} < 10^{-4} \text{ bar}$$



$$10^{-31} \text{ bar} < P_{O_2} < 10^{-15} \text{ bar}$$



Under oxygen-rich conditions,  $Cu^{3+}$  substitutions are charge compensated by both  $V_O^{\bullet\bullet}$  and  $Cu^{2+}$   $Cu_i^{\bullet}$ . Under oxygen-poor conditions, the  $Cu_i^{\bullet}$  are charge compensated by polarons as well as  $Cu_{Ce}''$ ,  $(Cu_{Ce,sq} - Ce_{Ce}')'''$ , and  $(Cu_{Ce}'' - V_O^{\bullet\bullet} - Ce_{Ce}')'$ . Therefore, the non-stoichiometry  $\delta$  is higher than in the undoped case under oxygen-rich conditions, whereas the polaron concen-

tration is higher than in the undoped case under oxygen-poor conditions.

The charge compensation mechanism can promote  $\delta$  and polaron concentration only in certain  $P_{O_2}$  ranges. In contrast, the formation of defect complexes increases non-stoichiometry and  $[Ce_{Ce}']$  concentration at whole  $P_{O_2}$  (when  $x > 10^{-3}$ ), as shown in Figure 8e,f. The non-stoichiometry  $\delta$  for  $x > 10^{-3}$  has a W-shaped dependence instead of a V-shaped dependence for  $x < 10^{-3}$ . This is because  $(Cu_{Ce}'' - V_O^{\bullet\bullet})^{\times}$  emerges at  $10^{-20} < P_{O_2} < 10^{-10}$ , which increases the overall vacancy concentration. When  $P_{O_2} < 10^{-20}$ ,  $(Cu_{Ce}'' - V_O^{\bullet\bullet} - Ce_{Ce}')'$  concentration is around 0.1% for  $x = 10^{-2}$ , which results in a higher  $\delta$ . Similarly, the occurrence of  $(Cu_{Ce,sq} - Ce_{Ce}')'''$  and  $(Cu_{Ce}'' - V_O^{\bullet\bullet} - Ce_{Ce}')'$  enhances polaron concentration. At  $10^{-5} < P_{O_2} < 10^{-5}$ , Cu is mostly an acceptor dopant, but these two defect complexes increase the polaron concentration.

**3.3. Implications for Catalytic Properties.** It is reasonable to assume that quantitatively the bulk defect equilibria and surface defect equilibria will differ. However, the changes in the surface adatom and substitutional defects as a function of

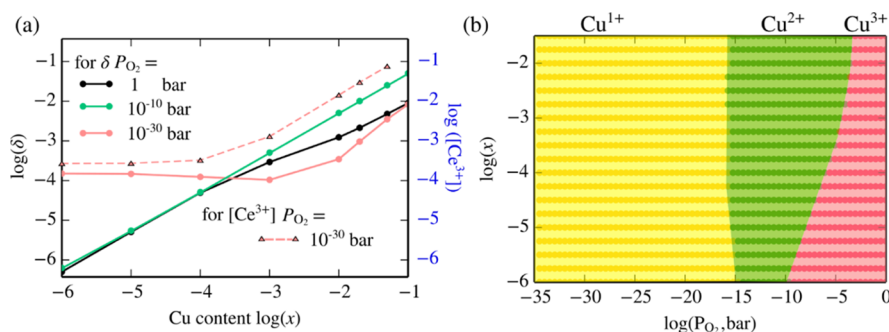


**Figure 9.** (a) Non-stoichiometry  $\delta$  at  $P_{O_2} = 1$  to  $10^{-30}$  bar, (b) dominant oxidation states of Cu, as a function of  $P_{O_2}$  in  $Cu_xCe_{1-x}O_{2-\delta}$  at 400 °C. In (b), yellow, green, and red dots represent the dominant oxidation state of Cu being 1+, 2+, and 3+, respectively. The dots are interpolated to construct the background color panels.

temperature and oxygen chemical potential can be qualitatively comparable to bulk interstitial and substitutional defects. That is, we expect the relative changes at the surface to follow the same trends as in the bulk behavior. The bulk charge compensation mechanism can be generalized to nanoparticle surfaces, except that the dominating regime for each mechanism may be shifted to a higher  $P_{O_2}$  because of easier reducibility of surface. Therefore, although the bulk defect chemistry cannot quantitatively represent what happens at Cu–CeO<sub>2</sub> surfaces, those results can still provide insights into how defect chemistry can affect catalytic activity at surfaces.

Under synthesis conditions (400 °C, 1 bar), Cu can increase the oxygen vacancy concentration. As shown in Figure 9a, the non-stoichiometry  $\delta$  increases at higher  $x$ . Typical WGS reaction conditions, that is, 2.73% CO, 23.37% CO<sub>2</sub>, 73.9% H<sub>2</sub>, 20 bar at 200 °C, are equivalent to  $P_{O_2} = 10^{-30}$  bar at 400 °C.<sup>39</sup> This effective oxygen partial pressure can be higher only if CO oxidation or water-splitting reactions are considered. In this reducing environment, the non-stoichiometry  $\delta$  is not linearly proportional to Cu content  $x$ . For  $x < 10^{-3}$ ,  $\delta$  is independent of  $x$  because the Cu-induced oxygen vacancies are negligible. For  $x > 10^{-3}$ ,  $\delta$  is higher at an increased  $x$ . Although the vacancy concentration is not as high as under oxygen-rich conditions, it is still 1–2 orders of magnitude higher than the undoped ceria. Because oxygen vacancies are active sites for H<sub>2</sub>O dissociation, a high concentration of oxygen vacancies can be beneficial for CO oxidation<sup>40,41</sup> and H<sub>2</sub>O dissociation<sup>6,42,43</sup> by increasing dissociative adsorption energy as well as stabilizing active surface metal species.

The polaron concentration in a reducing environment also increases in the presence of Cu interstitials. Figure 9a shows that low Cu content has no impact on polaron concentration in a reducing environment because the intrinsic vacancies are accompanied already by a significant amount of polarons. When the Cu doping level  $x$  is higher than  $10^{-3}$ , the polaron concentration starts to surpass that in the undoped ceria. For  $x = 10^{-2}$ , the polaron concentration in the Cu-doped ceria is around 30 times higher than that in the undoped case. This high polaron concentration can not only increase the electronic conductivity of the sample, but also offer extra in-gap states. These in-gap states, when available at surfaces, can promote O<sub>2</sub> adsorption,<sup>44</sup> proton adsorption,<sup>45</sup> and water splitting.<sup>46</sup>

Figure 9b shows that the dominant oxidation state changes from 3+ to 2+ and from 2+ to 1+ as  $P_{O_2}$  reduces. The reduction of Cu is consistent with experimental reports: Elias et al. observed Cu<sup>3+</sup> under oxygen-rich conditions (300 °C, 2.5% O<sub>2</sub>,

1% CO);<sup>13</sup> Si et al. observed Cu<sup>2+</sup> at low temperature (32 °C 5% CO/3% H<sub>2</sub>O) and Cu<sup>1+</sup> at higher temperature (250 °C 5% CO/3% H<sub>2</sub>O).<sup>47</sup> Under WGS conditions, the dominant oxidation state is 1+. A substantial amount ( $\sim 0.1\%$  for  $x = 1\%$ ) of Cu<sup>2+</sup> also appears. The transition between the 2+ and 1+ states can also participate in surface charge transfer, which may facilitate surface reactions.

#### 4. CONCLUSIONS

In summary, the Cu defect configurations and oxidation states were investigated for equilibrium and non-equilibrium Cu–CeO<sub>2</sub> systems. Because of the high formation energy of the Cu defects, the equilibrium Cu defect concentrations are very low, indicating no solid solution of Cu can form in ceria at equilibrium at the synthesis conditions of Cu–CeO<sub>2</sub> nanoparticle specimens reported in the literature. However, in experimental conditions (high Cu chemical potential and low temperature), non-equilibrium states with a high Cu content can be formed. In these non-equilibrium states, Cu acts as an acceptor substitutional dopant at high  $P_{O_2}$ , with a 3+ oxidation state. This defect is charge compensated by oxygen vacancies that are many orders of magnitude higher than that of the undoped ceria. At a lower  $P_{O_2}$ , the Cu converts to a 2+ substitution. At even lower  $P_{O_2}$  (i.e., WGS reactions  $P_{O_2} = 10^{-30}$ ), Cu becomes a 1+ interstitial donor dopant, charge compensating with polarons. When the Cu content is lower than  $10^{-4}$  per unit formula, the non-stoichiometry and polaron concentration is the same as in the undoped case. When Cu content exceeds  $10^{-3}$ , the non-stoichiometry can be 10 times higher than in the undoped case because of the formation of defect complexes. At this high doping level, there is substantial amount of acceptor substitutional dopant Cu bound with oxygen vacancies even under reducing conditions. At the same time, the polaron concentration can be enhanced by 30 times to charge compensate the Cu interstitials. Because oxygen vacancies and polarons are beneficial for surface activity, in particular water adsorption and dissociation, the Cu-enhanced oxygen vacancy concentration under WGS conditions can catalyze the reactions more effectively. Moreover, the Cu-oxidation state can be 1+ (dominant defect, about 90%) and 2+ (about 10%) under such conditions. The oxidation/reduction of the Cu species itself can also facilitate surface reactions.

This study shows that by considering all possible oxidation states and simple defect–defect interactions in the ceria, one can resolve the dominant defect species and explain why a higher Cu content can lead to a higher catalytic activity. The framework is

applicable to other transition metal-doped ceria systems. Moreover, this knowledge of bulk defect chemistry is a good starting point for further explicit calculations of surface defect species on Cu–CeO<sub>2</sub> nanoparticle catalysts.

## ■ ASSOCIATED CONTENT

### ● Supporting Information

The Supporting Information is available free of charge on the ACS Publications website at DOI: 10.1021/acs.jpcc.8b08222.

Test of different *U* values, configurations for simulation cell, volume change for each defect, notes on defect chemistry, notes on chemical potential reference, benchmark with experiment for undoped ceria (PDF)

## ■ AUTHOR INFORMATION

### Corresponding Author

\*E-mail: byildiz@mit.edu. Phone: 617-324-4009.

### ORCID

Lixin Sun: 0000-0002-7971-5222

Bilge Yildiz: 0000-0002-2688-5666

### Notes

The authors declare no competing financial interest.

## ■ ACKNOWLEDGMENTS

This research was supported by DOE-Basic Energy Sciences, grant number DE-SC0002633, and the National Science Foundation for computational support through the XSEDE Science Gateways program, grant number TGDMR120025.

## ■ REFERENCES

- (1) *Catalysis by Ceria and Related Materials*, 2nd ed.; Trovarelli, A., Fornasiero, P., Eds.; Catalytic Science Series; Imperial College Press: London, 2013.
- (2) Paier, J.; Penschke, C.; Sauer, J. Oxygen Defects and Surface Chemistry of Ceria: Quantum Chemical Studies Compared to Experiment. *Chem. Rev.* **2013**, *113*, 3949–3985.
- (3) Monte, M.; Gamarra, D.; Cámara, A. L.; Rasmussen, S. B.; Gyorffy, N.; Schay, Z.; Martínez-Arias, A.; Conesa, J. C. Preferential Oxidation of CO in Excess H<sub>2</sub> over CuO/CeO<sub>2</sub> Catalysts: Performance as a Function of the Copper Coverage and Exposed Face Present in the CeO<sub>2</sub> Support. *Catal. Today* **2014**, *229*, 104–113.
- (4) Liu, W.; Flytzani-Stephanopoulos, M. Transition Metal-Promoted Oxidation Catalysis by Fluorite Oxides: A Study of CO Oxidation over Cu–CeO<sub>2</sub>. *Chem. Eng. J. Biochem. Eng. J.* **1996**, *64*, 283–294.
- (5) Liu, W.; Flytzanistephanopoulos, M. Total Oxidation of Carbon Monoxide and Methane over Transition Metal Fluorite Oxide Composite Catalysts. *J. Catal.* **1995**, *153*, 304–316.
- (6) Wang, X.; Rodriguez, J. A.; Hanson, J. C.; Gamarra, D.; Martínez-Arias, A.; Fernández-García, M. In Situ Studies of the Active Sites for the Water Gas Shift Reaction over Cu–CeO<sub>2</sub> Catalysts: Complex Interaction between Metallic Copper and Oxygen Vacancies of Ceria. *J. Phys. Chem. B* **2006**, *110*, 428–434.
- (7) Li, Y.; Fu, Q.; Flytzani-Stephanopoulos, M. Low-Temperature Water-Gas Shift Reaction over Cu- and Ni-Loaded Cerium Oxide Catalysts. *Appl. Catal., B* **2000**, *27*, 179–191.
- (8) Hočevar, S.; Krašovec, U. O.; Orel, B.; Aricó, A. S.; Kim, H. CWO of Phenol on Two Differently Prepared CuO–CeO<sub>2</sub> Catalysts. *Appl. Catal., B* **2000**, *28*, 113–125.
- (9) Lu, Z.; Yang, Z.; He, B.; Castleton, C.; Hermansson, K. Cu-Doped Ceria: Oxygen Vacancy Formation Made Easy. *Chem. Phys. Lett.* **2011**, *510*, 60–66.
- (10) Kehoe, A. B.; Scanlon, D. O.; Watson, G. W. Role of Lattice Distortions in the Oxygen Storage Capacity of Divalently Doped CeO<sub>2</sub>. *Chem. Mater.* **2011**, *23*, 4464–4468.
- (11) Bera, P.; Priolkar, K. R.; Sarode, P. R.; Hegde, M. S.; Emura, S.; Kumashiro, R.; Lalla, N. P. Structural Investigation of Combustion Synthesized Cu/CeO<sub>2</sub> Catalysts by EXAFS and Other Physical Techniques: Formation of a Ce<sub>1-x</sub>Cu<sub>x</sub>O<sub>2-δ</sub> Solid Solution. *Chem. Mater.* **2002**, *14*, 3591–3601.
- (12) Wang, X.; Rodriguez, J. A.; Hanson, J. C.; Gamarra, D.; Martínez-Arias, A.; Fernández-García, M. Unusual Physical and Chemical Properties of Cu in Ce<sub>1-x</sub>Cu<sub>x</sub>O<sub>2</sub> Oxides. *J. Phys. Chem. B* **2005**, *109*, 19595–19603.
- (13) Elias, J. S.; Artrith, N.; Bugnet, M.; Giordano, L.; Botton, G. A.; Kolpak, A. M.; Shao-Horn, Y. Elucidating the Nature of the Active Phase in Copper/Ceria Catalysts for CO Oxidation. *ACS Catal.* **2016**, *6*, 1675–1679.
- (14) Fronzi, M.; Piccinin, S.; Delley, B.; Traversa, E.; Stampfl, C. Water Adsorption on the Stoichiometric and Reduced CeO<sub>2</sub> (111) Surface: A First-Principles Investigation. *Phys. Chem. Chem. Phys.* **2009**, *11*, 9188–9199.
- (15) Henderson, M. A.; Epling, W. S.; Perkins, C. L.; Peden, C. H. F.; Diebold, U. Interaction of Molecular Oxygen with the Vacuum-Annealed TiO<sub>2</sub> (110) Surface: Molecular and Dissociative Channels. *J. Phys. Chem. B* **1999**, *103*, 5328–5337.
- (16) Si, R.; Raitano, J.; Yi, N.; Zhang, L.; Chan, S.-W.; Flytzani-Stephanopoulos, M. Structure Sensitivity of the Low-Temperature Water-Gas Shift Reaction on Cu–CeO<sub>2</sub> Catalysts. *Catal. Today* **2012**, *180*, 68–80.
- (17) Jiang, S. P. A review of wet impregnation-An alternative method for the fabrication of high performance and nano-structured electrodes of solid oxide fuel cells. *Mater. Sci. Eng., A* **2006**, *418*, 199–210.
- (18) Zerva, C.; Philippopoulos, C. J. Ceria Catalysts for Water Gas Shift Reaction: Influence of Preparation Method on Their Activity. *Appl. Catal., B* **2006**, *67*, 105–112.
- (19) Rao, G. R.; Sahu, H. R.; Mishra, B. G. Surface and catalytic properties of Cu-Ce-O composite oxides prepared by combustion method. *Colloids Surf., A* **2003**, *220*, 261–269.
- (20) Knauth, P.; Saltsburg, H.; Engel, J.; Tuller, H. L. In Situ Dilatometric and Impedance Spectroscopic Study of Core–Shell like Structures: Insights into the Exceptional Catalytic Activity of Nanocrystalline Cu-Doped CeO<sub>2</sub>. *J. Mater. Chem. A* **2015**, *3*, 8369–8379.
- (21) Freysoldt, C.; Grabowski, B.; Hickel, T.; Neugebauer, J.; Kresse, G.; Janotti, A.; Van de Walle, C. G. First-Principles Calculations for Point Defects in Solids. *Rev. Mod. Phys.* **2014**, *86*, 253–305.
- (22) Kresse, G.; Joubert, D. From Ultrasoft Pseudopotentials to the Projector Augmented-Wave Method. *Phys. Rev. B: Condens. Matter Mater. Phys.* **1999**, *59*, 1758–1775.
- (23) Kresse, G.; Hafner, J. Ab initio molecular dynamics for liquid metals. *Phys. Rev. B: Condens. Matter Mater. Phys.* **1993**, *47*, 558–561.
- (24) Kresse, G.; Hafner, J. Ab initio molecular-dynamics simulation of the liquid-metal-amorphous-semiconductor transition in germanium. *Phys. Rev. B: Condens. Matter Mater. Phys.* **1994**, *49*, 14251–14269.
- (25) Perdew, J. P.; Wang, Y. Accurate and Simple Analytic Representation of the Electron-Gas Correlation Energy. *Phys. Rev. B: Condens. Matter Mater. Phys.* **1992**, *45*, 13244–13249.
- (26) Perdew, J. P.; Burke, K.; Ernzerhof, M. Generalized Gradient Approximation Made Simple. *Phys. Rev. Lett.* **1996**, *77*, 3865–3868.
- (27) Anisimov, V. I.; Aryasetiawan, F.; Lichtenstein, A. I. First-principles calculations of the electronic structure and spectra of strongly correlated systems: the LDA+U method. *J. Phys.: Condens. Matter* **1997**, *9*, 767.
- (28) Anisimov, V. I.; Zaanen, J.; Andersen, O. K. Band theory and Mott insulators: Hubbard U instead of Stoner I. *Phys. Rev. B: Condens. Matter Mater. Phys.* **1991**, *44*, 943–954.
- (29) Dudarev, S. L.; Botton, G. A.; Savrasov, S. Y.; Szotek, Z.; Temmerman, W. M.; Sutton, A. P. Electronic Structure and Elastic Properties of Strongly Correlated Metal Oxides from First Principles: LSDA + U, SIC-LSDA and EELS Study of UO<sub>2</sub> and NiO. *Phys. Status Solidi A* **1998**, *166*, 429–443.
- (30) Marrocchelli, D.; Bishop, S. R.; Tuller, H. L.; Watson, G. W.; Yildiz, B. Charge Localization Increases Chemical Expansion in

Cerium-Based Oxides. *Phys. Chem. Chem. Phys.* **2012**, *14*, 12070–12074.

(31) Wang, L.; Maxisch, T.; Ceder, G. Oxidation Energies of Transition Metal Oxides within the GGA+U Framework. *Phys. Rev. B: Condens. Matter Mater. Phys.* **2006**, *73*, 195107.

(32) Keating, P. R. L.; Scanlon, D. O.; Morgan, B. J.; Galea, N. M.; Watson, G. W. Analysis of Intrinsic Defects in CeO<sub>2</sub> Using a Koopmans-Like GGA+U Approach. *J. Phys. Chem. C* **2012**, *116*, 2443–2452.

(33) Nolan, M.; Watson, G. W. The Surface Dependence of CO Adsorption on Ceria. *J. Phys. Chem. B* **2006**, *110*, 16600–16606.

(34) Allen, J. P.; Watson, G. W. Occupation Matrix Control of D- and f-Electron Localisations Using DFT+U. *Phys. Chem. Chem. Phys.* **2014**, *16*, 21016.

(35) Zacherle, T.; Schriever, A.; De Souza, R. A.; Martin, M. Ab Initio Analysis of the Defect Structure of Ceria. *Phys. Rev. B: Condens. Matter Mater. Phys.* **2013**, *87*, 134104.

(36) Momma, K.; Izumi, F. VESTA 3 for three-dimensional visualization of crystal, volumetric and morphology data. *J. Appl. Crystallogr.* **2011**, *44*, 1272–1276.

(37) Humphrey, W.; Dalke, A.; Schulten, K. VMD: Visual Molecular Dynamics. *J. Mol. Graphics* **1996**, *14*, 33–38.

(38) Vanpoucke, D. E. P.; Bultinck, P.; Cottenier, S.; Van Speybroeck, V.; Van Driessche, I. Aliovalent Doping of CeO<sub>2</sub>: DFT Study of Oxidation State and Vacancy Effects. *J. Mater. Chem. A* **2014**, *2*, 13723–13737.

(39) Ovesen, C. V.; Clausen, B. S.; Hammershøj, B. S.; Steffensen, G.; Askgaard, T.; Chorkendorff, I.; Nørskov, J. K.; Rasmussen, P. B.; Stoltze, P.; Taylor, P. A Microkinetic Analysis of the Water-Gas Shift Reaction under Industrial Conditions. *J. Catal.* **1996**, *158*, 170–180.

(40) Ghosh, P.; Camellone, M. F.; Fabris, S. Fluxionality of Au Clusters at Ceria Surfaces during CO Oxidation: Relationships among Reactivity, Size, Cohesion, and Surface Defects from DFT Simulations. *J. Phys. Chem. Lett.* **2013**, *4*, 2256–2263.

(41) Huang, M.; Fabris, S. CO Adsorption and Oxidation on Ceria Surfaces from DFT+U Calculations. *J. Phys. Chem. C* **2008**, *112*, 8643–8648.

(42) Molinari, M.; Parker, S. C.; Sayle, D. C.; Islam, M. S. Water Adsorption and Its Effect on the Stability of Low Index Stoichiometric and Reduced Surfaces of Ceria. *J. Phys. Chem. C* **2012**, *116*, 7073–7082.

(43) Rodriguez, J. A.; Ma, S.; Liu, P.; Hrbek, J.; Evans, J.; Perez, M. Activity of CeO<sub>x</sub> and TiO<sub>x</sub> Nanoparticles Grown on Au(111) in the Water-Gas Shift Reaction. *Science* **2007**, *318*, 1757–1760.

(44) Setvin, M.; Daniel, B.; Aschauer, U.; Hou, W.; Li, Y.-F.; Schmid, M.; Selloni, A.; Diebold, U. Identification of Adsorbed Molecules via STM Tip Manipulation: CO, H<sub>2</sub>O, and O<sub>2</sub> on TiO<sub>2</sub> Anatase (101). *Phys. Chem. Chem. Phys.* **2014**, *16*, 21524–21530.

(45) Selcuk, S.; Selloni, A. Facet-Dependent Trapping and Dynamics of Excess Electrons at Anatase TiO<sub>2</sub> Surfaces and Aqueous Interfaces. *Nat. Mater.* **2016**, *15*, 1107.

(46) Chueh, W. C.; McDaniel, A. H.; Grass, M. E.; Hao, Y.; Jabeen, N.; Liu, Z.; Haile, S. M.; McCarty, K. F.; Bluhm, H.; El Gabaly, F. Highly Enhanced Concentration and Stability of Reactive Ce<sup>3+</sup> on Doped CeO<sub>2</sub> Surface Revealed In Operando. *Chem. Mater.* **2012**, *24*, 1876–1882.

(47) Marrocchelli, D.; Bishop, S. R.; Kilner, J. Chemical Expansion and Its Dependence on the Host Cation Radius. *J. Mater. Chem. A* **2013**, *1*, 7673.